

Electronic structure and thermoelectric properties of *n*- and *p*-type SnSe from first principles calculations

K. Kutorasinski,* B. Wiendlocha, S. Kaprzyk, and J. Tobola
 AGH University of Science and Technology, Faculty of Physics and
 Applied Computer Science, Al. Mickiewicza 30, 30-059 Krakow, Poland
 (Dated: April 28, 2015)

We present results of the electronic band structure, Fermi surface and electron transport properties calculations in the orthorhombic *n*- and *p*-type SnSe, applying the Korringa-Kohn-Rostoker method and the Boltzmann transport approach. The analysis accounted for the temperature effect on crystallographic parameters in *Pnma* structure as well as the phase transition to *CmCm* structure at $T_c \sim 807$ K. Remarkable modifications of the conduction and valence bands were notified upon varying crystallographic parameters within the structure before T_c , while the phase transition mostly leads to the jump in the band gap value. The diagonal components of the kinetic parameter tensors (velocity, effective mass) and resulting transport quantity tensors (electrical conductivity σ , thermopower S and power factor PF) were computed in a wide range of temperature (15 – 900 K), and hole (*p*-type) and electron (*n*-type) concentrations ($10^{17} - 10^{21} \text{ cm}^{-3}$). SnSe is shown to have a strong anisotropy of the electron transport properties for both types of charge conductivity, as expected for the layered structure, with the generally heavier *p*-type effective masses, comparing to *n*-type ones. Interestingly, *p*-type SnSe has strongly non-parabolic dispersion relations, with the 'pudding-mold'-like shape of the highest valence band. The analysis of σ , S and PF tensors indicates, that the inter-layer electron transport is beneficial for thermoelectric performance in *n*-type SnSe, while this direction is blocked in *p*-type SnSe, where in-plane transport is preferred. Our results predict, that the *n*-type SnSe is potentially even better thermoelectric material than the *p*-type one. Theoretical results are compared with the single crystal *p*-SnSe measurements, and a good agreement is found below 600 K. The discrepancy between the computational and experimental data, appearing at higher temperatures, can be explained assuming an increase of the hole concentration vs. T , which is correlated with the experimental Hall data.

I. INTRODUCTION

Thermoelectric (TE) conversion in crystalline solids constantly attracts the interest of scientists, not only due to the increasing performance of energy harvesting systems, but also due to the fact that the conventional and 'well-known' thermoelectric materials, such as PbX ($X = \text{S, Se, Te}$)²⁻⁴ or Bi_2Te_3 (e.g.⁵), still surprise by their novel and remarkable physical behaviors. It is commonly accepted, that TE figure of merit $zT = \sigma S^2 / \kappa T$ well captures basic transport properties of the material at given temperature T , i.e. electrical conductivity (σ), Seebeck coefficient (S) and thermal conductivity (κ), and is conveniently expressed in dimensionless units. As all these transport quantities apparently depend on temperature and carrier concentration (n or p), the maximum of zT is expected when properly correlating both intrinsic electron transport properties of the system (e.g. the band gap magnitude) with temperature range, and doping level with the hole or electron concentration, to achieve *p*- or *n*-type materials, respectively. But, getting a better insight into atomic-level connections among crystal stability, electronic and lattice properties of TE systems generally allow for a more convinced interpretation of the complex transport phenomena.

Recent experimental work¹ reported $zT \sim 2.6$ at $T \sim 920$ K, along one of the axis in the single crystal *p*-type SnSe, which classified this well-known semiconductor as a very promising TE material. However, fur-

ther results^{7,8} revealed much lower zT for polycrystalline samples, showing that SnSe is a rather complex system.

SnSe is a layered material, with an orthorhombic symmetry of the unit cell, and its crystal structure strongly depends on temperature. First of all, SnSe exhibits a crystallographic phase transition at $T_c = 807$ K.⁶ Below T_c , its unit cell can be described in the *Pnma* simple orthorhombic space group No. 62, with 4 chemical formulas (8 atoms) in the unit cell (see, Fig. 1). Crystal structure parameters of this 'low temperature' (i.e. below T_c) phase depend on temperature as well⁶. Since the temperature dependence of the transport properties (e.g. thermopower) is discussed in our work, those changes in crystal structure were also taken into account. Accordingly, three cases are considered: low-temperature (LT)

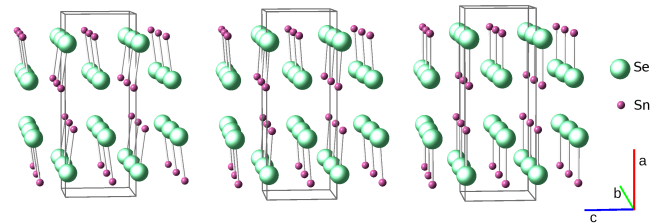


FIG. 1: (Color online) Crystal structure of SnSe (Se - large, green balls, Sn- small, magenta). Left: LT phase (*Pnma* at 295 K); center: MT "phase" (*Pnma* at 790 K); right: HT phase (*Pbmm* above 807 K).

phase, described by the experimental crystallographic data taken at $T_{\text{expt}} = 295$ K, and used in our calculations to represent SnSe in the temperature range $T_{\text{calc}} = 10 - 550$ K; mid-temperature (MT) phase ($T_{\text{expt}} = 790$ K and $T_{\text{calc}} = 550 - 807$ K); and high-temperature (HT) phase ($T_{\text{expt}} = 829$ K and $T_{\text{calc}} > 807$ K), as displayed in the Table I. Above T_c , the high-temperature phase has an orthorhombic c -base centered $CmCm$ space group (No. 63). The transition from the simple to the centered unit cell reduces the number of atoms in the primitive cell, from 8 to 4, changing the shape and size of the Brillouin zone (BZ). Thus, it becomes impossible to directly compare the electronic dispersion relations between the LT/MT and HT phases, if using the HT centered unit cell. Therefore, to allow for a better understanding, and easier analysis of the role of the phase transition in the evolution of the electronic structure and transport properties of SnSe, we transformed the HT SnSe centered unit cell into the equivalent $Pbmm$ simple orthorhombic one (No. 51). $Pbmm$ unit cell has the same number of atoms and similar alignment of the unit cell axes, as the structure before the transition (i.e. a axis is the longest, b is the shortest, and c is in between, see, Fig. 1). With this transformation, the Brillouin zone and location of the high symmetry points remain similar in both phases (small changes are only in BZ dimensions, due to lattice parameters' variation). In our computations, the actual values of lattice parameters for HT phase were taken from the high temperature ($T = 829$ K) neutron measurements⁶, and are shown in the Table. I. It is worth noting that the crystal structure of SnSe evolves smoothly with temperature (even while crossing T_c) and the unit cell dimensions, as well as interatomic distances, change rather continuously with temperature (see, Table I and Ref. 6). The crystal structure parameter, which exhibits the most rapid change at T_c , is the z parameter positioning Sn and

Se atoms.

Recently, first principles calculations of transport properties of p -type SnSe were reported in Ref. 9. In our work we give more extended analysis of the electronic structure, effective masses and transport properties of both, n - and p -type, SnSe. The constant relaxation time approximation is used, and phonon drag effects are not discussed.

The paper is organized as follows. In Sec. II theoretical and computational details are presented. Sec. III A describes in details the electronic band structure and the Fermi surface of the valence and conduction states, together with the effective mass and the transport function analysis. Sec. III B discusses anisotropic (single crystal) and isotropic (polycrystalline-like) transport properties in function of temperature and carrier concentration, and comparison with experimental data is done. Sec. IV contains summary and conclusions of the work. In Appendix A, formulas for averaging of the anisotropic transport coefficients, in order to compute their isotropic (polycrystalline) analogs, are derived. Appendix B contains complementary data.

II. THEORETICAL DETAILS

A. Thermopower

The Boltzmann transport theory¹⁰⁻¹², successfully applied to study transport properties of various crystalline materials¹³⁻¹⁵ is used to calculate the energy-dependent electrical conductivity $\sigma(\mathcal{E})$ (so-called transport function, TF):

$$\sigma(\mathcal{E}) = e^2 \sum_n \int \frac{d\mathbf{k}}{4\pi^3} \tau_n(\mathbf{k}) \mathbf{v}_n(\mathbf{k}) \otimes \mathbf{v}_n(\mathbf{k}) \delta(\mathcal{E} - \mathcal{E}_n(\mathbf{k})). \quad (1)$$

Symbol \otimes represents outer product (Kronecker product) of two vectors, $\mathbf{v}_n(\mathbf{k}) = \nabla_{\mathbf{k}} \mathcal{E}_n(\mathbf{k})$ and $\tau_n(\mathbf{k})$ is a velocity and life time of electrons on band $\mathcal{E}_n(\mathbf{k})$, respectively. The transport function tensor has to be reformulated into the form, that is more convenient for the numerical computation. With the use of the constant relaxation time approximation ($\tau_n(\mathbf{k}) = \tau_0$), and after changing 3D \mathbf{k} -space integration to the 2D surface integration ($\mathcal{E}_n(\mathbf{k}) \rightarrow S_n(\mathcal{E})$) it takes the form:

$$\sigma_\tau(\mathcal{E}) = \tau_0 \frac{e^2}{\hbar} \sum_n \int_{S_n(\mathcal{E})} \frac{dS}{4\pi^3} \frac{\mathbf{v}(S_n(\mathcal{E})) \otimes \mathbf{v}(S_n(\mathcal{E}))}{|\mathbf{v}(S_n(\mathcal{E}))|}. \quad (2)$$

TF is directly related to the macroscopic transport coefficients, like thermopower, electronic part of thermal conductivity or electrical conductivity. Within this approach¹⁰ the two basic transport tensors (electrical conductivity σ_e and thermopower \mathbf{S}) can be expressed as

$$\sigma_e = \mathcal{L}^{(0)}, \quad \mathbf{S} = -\frac{1}{eT} \frac{\mathcal{L}^{(1)}}{\mathcal{L}^{(0)}}, \quad (3)$$

TABLE I: Crystallographic data⁶ of the SnSe compound, measured at different temperatures T_{expt} , used in our calculations for selected temperature ranges T_{calc} .

Phase, T range	Space group	Lattice const.(Å)	Atomic positions	
			Sn	Se
Low-T. (LT)	$Pnma$	$a = 11.501$	x: 0.6186	0.3551
$T_{\text{expt}} = 295$ K	No. 62	$b = 4.153$	y: 0.25	0.25
$T_{\text{calc}} < 550$ K		$c = 4.445$	z: 0.1032	0.4818
Mid-T. (MT)	$Pnma$	$a = 11.620$	x: 0.6230	0.3553
$T_{\text{expt}} = 790$ K	No. 62	$b = 4.282$	y: 0.25	0.25
$T_{\text{calc}} = 550-807$ K		$c = 4.334$	z: 0.0584	0.4878
High-T. (HT)	$Pbmm^a$	$a = 11.62$	x: 0.6248	0.3558
$T_{\text{expt}} = 829$ K	No. 51 ^a	$b = 4.282$	y: 0.25	0.25
$T_{\text{calc}} > 807$ K		$c = 4.293$	z: 0.00	0.50

^aTransformed from $CmCm$ (No. 61)

where

$$\mathcal{L}^{(\alpha)} = \int d\mathcal{E} \left(-\frac{\partial f}{\partial \mathcal{E}} \right) (\mathcal{E} - \mu_c)^\alpha \sigma(\mathcal{E}). \quad (4)$$

The value of the chemical potential $\mu_c = \mu_c(T, n_d)$ depends on the temperature (T), carrier concentration and the type of conductivity (n, p) (see, Sec. II C).

In case of the anisotropic structure, like the orthorhombic SnSe, transport function tensor (and thermopower as well) has three linearly independent elements, and in this work, diagonal elements (i.e. S_{xx} , S_{yy} , S_{zz}) are calculated. For the polycrystalline sample without texture, those three elements have to be averaged in a proper way, to obtain the macroscopically isotropic thermopower and power factor (PF). The relevant formulas are given here and derived in the Appendix A:

$$S_{\text{avg}} = \frac{S_{xx}\sigma_{xx} + S_{yy}\sigma_{yy} + S_{zz}\sigma_{zz}}{\sigma_{xx} + \sigma_{yy} + \sigma_{zz}}, \quad (5)$$

$$\text{PF}_{\text{avg}} = \frac{1}{3} (S_{xx}^2\sigma_{xx} + S_{yy}^2\sigma_{yy} + S_{zz}^2\sigma_{zz}). \quad (6)$$

Since the power factor, in the constant relaxation time approximation, depends linearly on the relaxation time τ (not calculated here), consequently PF divided by τ is presented.

B. DOS and effective mass

In a similar way to the transport function, the density of states (DOS) is calculated:

$$g(\mathcal{E}) = \sum_n \int_{S_n(\mathcal{E})} \frac{dS}{4\pi^3} \frac{1}{|\nabla_{\mathbf{k}} \mathcal{E}_n(\mathbf{k})|}. \quad (7)$$

With this definition $g(\mathcal{E})$ has the units of $\text{eV}^{-1}\text{m}^{-3}$, i.e. it includes the volume of the unit cell.

The DOS function is closely connected to the DOS effective mass, m^* . Here, energy dependent m^* is calculated using the formula¹⁵

$$m_{\text{DOS}}(\mathcal{E}) = m_e m_{\text{DOS}}^*(\mathcal{E}) = \hbar^2 \sqrt[3]{\pi^4 g(\mathcal{E}) g'(\mathcal{E})}. \quad (8)$$

Alternatively, effective mass can be computed by integrating the effective mass tensor, over the isoenergetic surfaces:

$$m_{ij}(\mathcal{E}) = m_e m_{ij}^*(\mathcal{E}) = \int_{S_n(\mathcal{E})} [\mathbf{M}_{ij}] dS \bigg/ \int_{S_n(\mathcal{E})} dS, \quad (9)$$

where the effective mass tensor is defined as¹⁰

$$[\mathbf{M}_{ij}]^{-1} = \frac{1}{\hbar^2} \frac{\partial^2 \mathcal{E}}{\partial k_i \partial k_j} \quad (10)$$

Using Eq. 9 and 10 one may discuss the direction dependence of the effective mass. In case of an orthorhombic structure with orthogonal axes, $[\mathbf{M}_{ij}]$ tensor is diagonal, and components m_{xx}^* , m_{yy}^* , m_{zz}^* are computed.

The isotropic band effective mass is determined by the geometrical mean

$$m_{iso}^* = \sqrt[3]{m_{xx}^* m_{yy}^* m_{zz}^*}. \quad (11)$$

Both ways of effective mass calculations (DOS effective mass from Eq. 8 and band effective mass from Eq. 11) give the same results only for parabolic bands. Difference of those two results gives opportunity to estimate the importance of non-parabolicity of the electronic band structure.

The aforementioned effective masses correspond to the $T = 0$ K temperature. The temperature effects can be taken into account via the Fermi-Dirac distribution function in a similar way, as in the thermopower calculation in Eq. 3. The actual number of 'active' (conducting) electrons, in temperature T , can be represented as $n_{\text{active}} = \int d\mathcal{E} g(\mathcal{E}) \left(-\frac{\partial f}{\partial \mathcal{E}} \right)$ and the effective mass of active electrons, as a function of temperature, can be determined from

$$m^*(T, n_d) = \frac{\int d\mathcal{E} m^*(\mathcal{E}) g(\mathcal{E}) \left(-\frac{\partial f}{\partial \mathcal{E}} \right)}{\int d\mathcal{E} g(\mathcal{E}) \left(-\frac{\partial f}{\partial \mathcal{E}} \right)}. \quad (12)$$

where n_d is the carrier concentration, at which m^* is calculated (see, Sec. II C). Note, that this analysis requires an assumption that effective mass is well defined, which for strongly non-parabolic bands may not be valid.

C. Doping and chemical potential

SnSe is an intrinsic semiconductor, where the Fermi energy lies inside the gap. As already mentioned, transport properties of the intrinsically (defect-doped) p -type single crystal¹, polycrystal⁷, and p -type Ag-doped polycrystal⁸ samples were reported. To simulate the behavior of the system after doping, we use the rigid band model²⁶. In this approach, additional number n_d of electrons or holes is the control parameter, added to mimic n -type (positive n_d) or p -type (negative n_d) behavior, and chemical potential $\mu_c = \mu_c(T, n_d)$ needed in Eq. (4) is calculated using the formula

$$n + n_d = \int d\mathcal{E} g(\mathcal{E}) \frac{1}{1 + \exp\left(\frac{\mathcal{E} - \mu_c(T, n_d)}{k_B T}\right)}. \quad (13)$$

n is the total number of valence electrons in the system (which is 10 per f.u. in case of SnSe) and the integral is taken from the bottom of the valence bands.

D. Band structure computational details

Electronic band structure calculations were performed using the full potential Korringa-Kohn-Rostoker^{16–21} (KKR) method, within the scalar relativistic approach^{22,23}. Local density approximation (LDA) parametrization of Perdew and Wang²⁷ was employed. The self-consistent cycle was repeated until the difference between the input and output potentials was less than 1 mRy in any point inside the unit cell. Isoenergetic surfaces $S_n(\mathcal{E})$ were obtained with the use of marching cube algorithm²⁴ on a mesh consisting of $80 \times 80 \times 80$ voxels. To improve visualization, vertex normal²⁵ and vertex color techniques were also used. All energy dependent functions were calculated with a resolution of 2.5 meV. The transport function was additionally interpolated between energy mesh points, using spline functions, which allows to obtain converged results for temperatures above 10 K, in the concentration range of $10^{17} - 10^{21} \text{ cm}^{-3}$.

III. RESULTS

A. Electronic Structure

Electronic dispersion relations are shown in Fig. 2, for the LT (Fig. 2a), MT (Fig. 2b) and HT (Fig. 2c) phases²⁹ of SnSe. As expected, local density approximation (LDA), used in this work, underestimated the band gaps. Since the gap value is the important parameter in transport properties calculations, especially in elevated temperatures, the computed band gaps were expanded to mimic the experimental ones (see Tab. II). For the LT phase, the band gap value was set to $E_g^{\text{exp}} = 0.86 \text{ eV}$ ¹. In MT and HT phases, where experimental data are not available, the calculated gap values were extrapolated proportionally as in the LT phase, i.e. we assume that the LDA underestimation is proportional to the real gap value. It is worth noting, that the calculated values of the energy gaps for the LT and MT phases are almost the same, whereas the HT phase has much smaller gap (see, Tab. II). To verify whether the reduction of the band gap is related to the change in atomic positions or the unit cell parameters, additional calculations were performed for the MT phase, using (i) the MT atomic parameters and HT lattice constants, and (ii) MT lattice constants and HT atomic parameters. The resulting LDA band gaps were: 0.465 eV and 0.355 eV, respectively, thus we found, that the gap value is controlled mainly by the Sn and Se atomic positions. Recent calculations⁹, using the GW method, reported $E_g = 0.829 \text{ eV}$ for the LT phase and 0.46 eV for HT, thus reduction of E_g after the phase transition was also found.

As we explained in the Introduction, due to the transformation of the HT crystal structure to the simple orthorhombic $Pbmm$ space group, Brillouin zones in all (LT, MT and HT) phases in our calculations have the same shape and high symmetry points (BZ is shown

schematically in Fig. 2). The reciprocal space x, y, z axes are parallel to the a, b, c real space directions. Let us start with some general comments of the band structure, before going into the detailed analysis of the effective masses and the transport properties. In the LT phase, the highest valence band (VB) appears in the $\Gamma - Z$ direction, parallel to the z axis. It is worth noting, that in the LT phase, this highest VB has a 'pudding mold'-like shape, reported to be beneficial for thermoelectric performance in other systems²⁸. For the higher temperature structures (MT and HT), valence bands are much different, which points out that electronic band structure is sensitive to temperature, as simulated by the unit cell changes. The 'pudding mold'-like VB changes the shape to become more parabolic, and the second VB at $\Gamma - Y$ direction, aligns to band in $\Gamma - Z$ direction. The lowest conduction band (CB), seen in the $\Gamma - Y$ direction in all phases, is parabollic-like. Above the band gap we see, that the whole band structure in the $\Gamma - Z$ direction considerably moves down, as going from LT to HT, which is correlated with the shortening of the corresponding unit cell c axis. In the LT structure, the in-plane unit cell parameters, $b = 4.153 \text{ \AA}$ and $c = 4.445 \text{ \AA}$ are significantly different, which in the reciprocal space is reflected in a different alignment of the $\Gamma - Y$ and $\Gamma - Z$ bands. After the phase transition, as well as in the MT case, $b \simeq c$, and the energy locations of CB's minima and VB's maxima become similar between those two directions. What seems quite surprising, the differences in the band structures between the LT and MT (both before the phase transition) are much larger than between the MT and HT structures (i.e. induced by the phase transition). This shows that the electronic structure evolves continuously with temperature, however the band gap changes abruptly at the phase transition (see, Tab. II), which can result in rapid changes in the transport properties.

It is also interesting to analyze the bands in $Z - U$ and $\Gamma - X$ directions, which represent the real-space a direction, i.e. contributing the charge transport between the SnSe layers. In all the cases, for the VB part, the resulting bands are very flat, which is quite intuitive, since we expect hampered charge propagation in this direction. On the other hand, conduction band in $\Gamma - X$ is very steep and almost linear. All these band structure features are reflected in the transport properties of SnSe, as discussed below.

TABLE II: Calculated (LDA) and experimental¹ values of the energy band gap (in eV) in SnSe for the three structures, LT, MT and HT.

Structure	LDA	Experimental	Used
LT	0.474	0.86 ^a	0.86
MT	0.487	no data	0.87
HT	0.350	no data	0.64

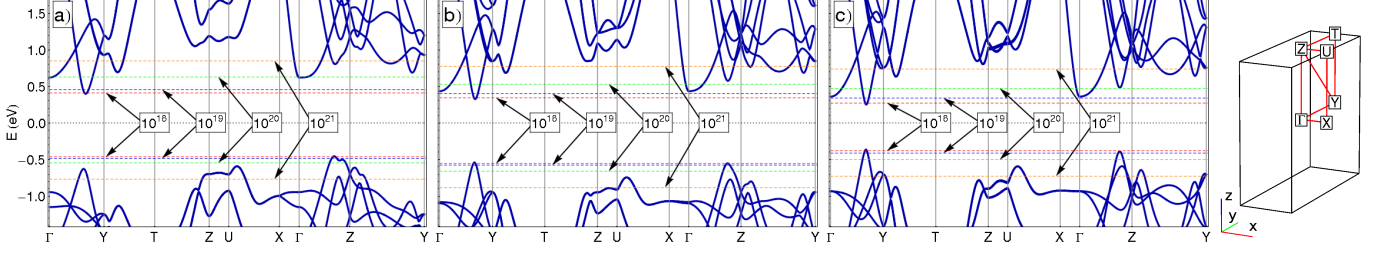


FIG. 2: (Color online) Electronic band structure of the LT (a), MT (b), and HT (c) phases of SnSe, computed along the high symmetry directions, as shown in the orthorhombic Brillouin zone. Horizontal lines mark the Fermi energy positions (μ_c at $T = 0$ K)

for the electron/hole concentration (in cm^{-3}) of $n = 10^{18}$ (red), $n = 10^{19}$ (blue), $n = 10^{20}$ (green) and $n = 10^{21}$ (orange), respectively.

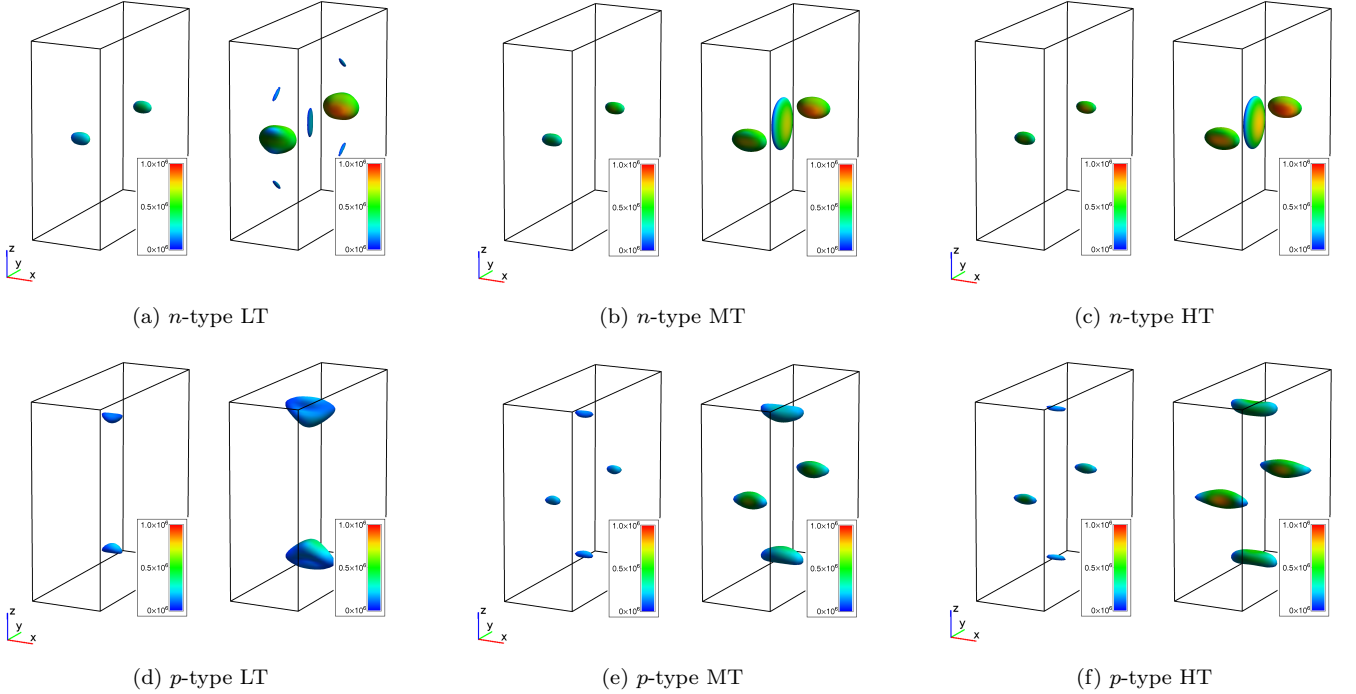


FIG. 3: (Color online) Fermi surfaces of the LT (a,d), MT (b,e) and HT (c,f) phases of SnSe, for the n -type (a-c) and p -type (d-f) doping, for the carrier concentration (in cm^{-3}) 10^{19} (left sub-panel) and 10^{20} (right sub-panel).

Electron velocities (in m/s) are represented by a color scale.

1. n -type doping

For the n -type doping (whatever the LT, MT and HT structures) at electron concentrations $< 10^{19} \text{ cm}^{-3}$, Fermi level reaches one ellipsoidal electron pocket (with two-fold degeneracy) in Γ -Y direction (see Fig. 2 and Fig. 3 a,b,c). The band, forming this pocket, has a regular, parabolic-like shape, and isotropic effective mass equals $m_{iso}^* \simeq 0.3 - 0.4$ in LT, and $m_{iso}^* \simeq 0.2 - 0.3$ in MT and HT case, respectively. The highest values of m^* are found along the x -direction (see Fig. 4b,d,f), where they quickly exceed $m_{xx}^* \simeq 0.5$. Therefore, velocity integrated over the Fermi surface (i.e. transport function),

is 3 times lower in the x -direction than in the y - and z -directions (see. Fig. 5b,d,f), and low x -direction electrical conductivity is expected (since $\sigma_e \sim \sigma(\mathcal{E}_F)$). This behavior corresponds to our expectations of the lower electrical conductivity perpendicular to SnSe layers (x -direction is along a -axis). Electron transport properties change dramatically when the Fermi level reaches further electron pockets; one in HT and MT at the Γ point, at $\sim 10^{19} \text{ cm}^{-3}$, and five in the LT structure (one centered at the Γ point and four in the Γ -T direction) at $\sim 10^{20} \text{ cm}^{-3}$. At these concentrations, the aforementioned steep linear band in $\Gamma - X$ is activated. In contrast to the previous case, these new pockets have the

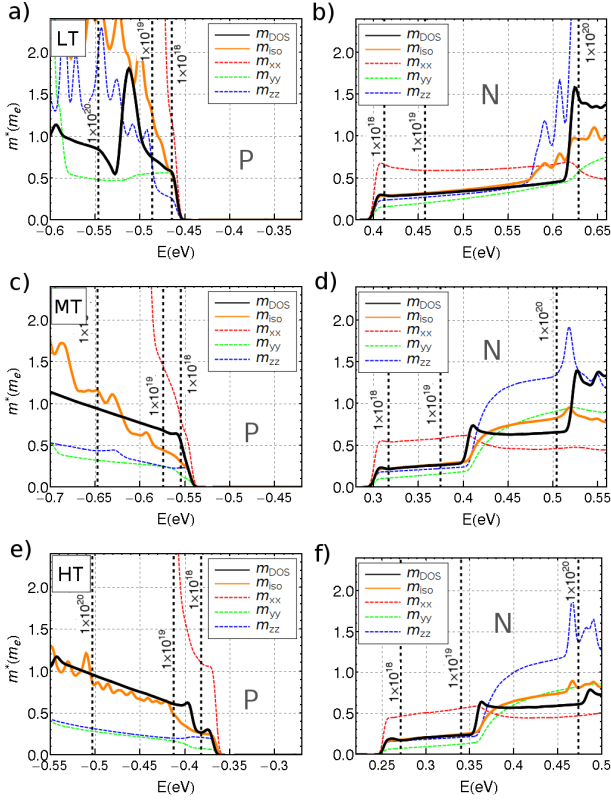


FIG. 4: (Color online) Effective mass of the LT (a,b), MT (c,d) and HT (e,f) phases of SnSe, calculated using Eq. 8 (m_{DOS}), Eq. 9 (m_{xx} , m_{yy} and m_{zz}) and Eq. 11 (m_{iso}). In each case, zero energy is fixed to the middle of the energy gap. Black vertical lines show the Fermi level for various carrier concentrations (in cm^{-3}) 1×10^{18} , 1×10^{19} and 1×10^{20} . Left and right columns present results for the p -type and n -type doping, respectively.

smallest m_{xx} (see Fig. 4), while the largest mass tensor component is now m_{zz} . In consequence, the average effective mass, represented by m_{iso}^* or m_{DOS}^* , raises rapidly to $1.0 - 1.5$ (for $n \sim 10^{20} \text{ cm}^{-3}$ in LT), and $0.6 - 0.9$ (for $n \sim 10^{19} \text{ cm}^{-3}$ in HT and MT). Thus, the transport function tensor component σ_{xx} (Fig. 5b,d) changes from the smallest, in energy range corresponding to the electron concentration below 10^{19} cm^{-3} , to the largest, at energies corresponding to 10^{20} cm^{-3} . The rapid increase of the σ_{xx} (connected to the alignment of the five pockets at the same energy) should favor the high thermopower S_{xx} , since $S \sim d(\ln \sigma)/d\mathcal{E}$. In case of the n -type doping, in the LT, MT and HT phases, after reaching certain concentration between 10^{19} cm^{-3} (HT) - 10^{20} cm^{-3} (LT, see, Fig. 5) two types of electrons are involved in the electrical transport along the x -direction: first, those having low mass and high velocity, providing high conductivity, and second, heavy electrons that are needed to achieve high thermopower. In such a case large power factor can be expected.

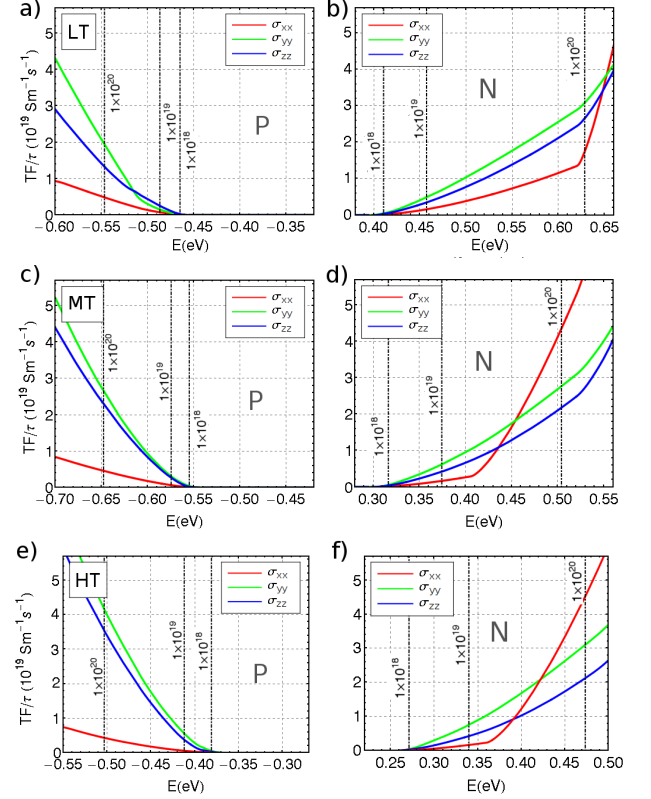


FIG. 5: (Color online) Transport Function (TF) of valence and conduction bands in LT, MT and HT phases of SnSe. Zero energy is fixed in the middle of energy gap, as in Fig. 2. Black vertical lines show Fermi level for various carrier concentration (in cm^{-3}): 1×10^{18} , 1×10^{19} and 1×10^{20} . Left and right columns present results for p -type and n -type doping, respectively.

DOS effective mass, plotted as a function of the carrier concentration and temperature (temperature effects according to Eq. 12), is shown in Fig. 6. For a sake of completeness, we present results for all the phases (LT, MT and HT) in the wide $15 - 900 \text{ K}$ temperature range. Appearance of the additional electron pockets, that is manifested in the rapid rise of the effective mass, have sharply determined concentrations only at very low temperatures. For $T = 300 \text{ K}$, due to temperature blurring of the Fermi-Dirac statistics, m^* changes gradually with a pronounced bump above 10^{20} cm^{-3} in the LT structure. At temperature c.a. $T = 800 \text{ K}$ or higher, electrons, which actively conduct, presumably come from the deeper lying bands, that have strongly non-parabolic dispersion relations. Thus, effective mass is not well defined, and the results must be treated with caution. Generally, in all the phases, DOS effective masses rise with the concentration, from approximately $0.3 m_e$ at $n = 10^{18} \text{ cm}^{-3}$ to $2 - 3 m_e$ at $n = 10^{21} \text{ cm}^{-3}$.

2. *p*-type doping

In the *p*-type LT-structure, up to 10^{20} cm^{-3} , the Fermi level penetrates hole pockets located in Γ -Z direction (Fig. 3d). These pockets have non-ellipsoidal shape, which is caused by the 'pudding-mold'-like band, having two maxima (see Fig. 2a). In this case, effective mass cannot be well defined (see Fig. 6a), since such a band exhibits both, electron-like, and hole-like properties, due to the convex and concave curvatures. However, the Fermi surface shape indicates, that the *x*-direction effective mass possesses the highest value (elongated shape in *x*-direction), which, in real space, corresponds to the *a*-axis direction (perpendicular to the SnSe layers). This behavior obviously affects the carrier velocity, integrated over the Fermi surface (see, Fig. 5a). The component σ_{xx} , similar to *n*-type case, is again the lowest and the highest values of TF are detected in *z*- (close to VB edge) and *y*-directions (well below VB edge), both being parallel to the SnSe atomic layers. Interestingly, at higher temperatures (MT and HT phases) the bands in Γ -Z direction do not have inflection, and the effective mass is therefore well defined. At higher concentrations ($10^{20} - 10^{21} \text{ cm}^{-3}$) in LT, the Fermi level also reaches holes from the Γ -Y direction (see Fig. 2a and Fig. 3a). In HT (and also MT), the axial anisotropy of the transport properties of SnSe (m^* and TF) is nicely visible: very large effective mass

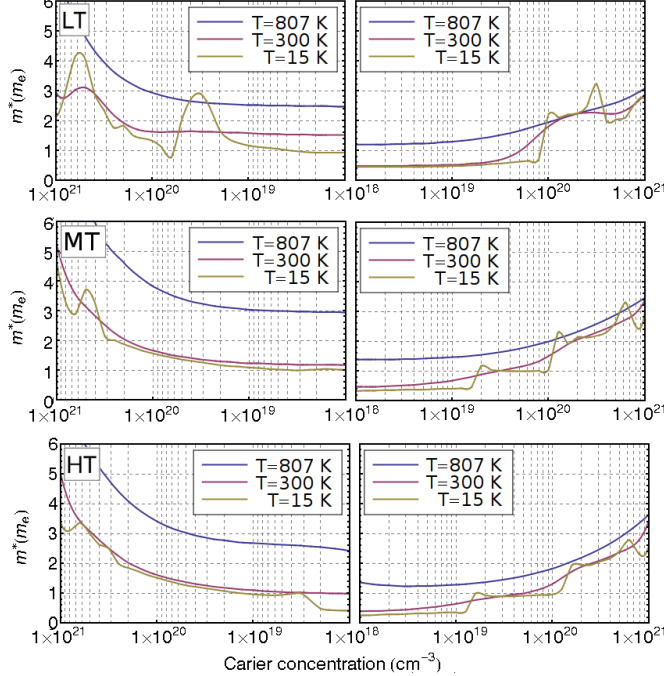


FIG. 6: (Color online) DOS effective mass in function of the carrier concentration and temperature for the LT, MT and HT phases of SnSe. Left and right columns correspond to the *p*-type and *n*-type doping, respectively.

and the smallest transport function is seen in *x*-direction, compared to much more 'conducting' *y*- and *z*-directions (in-plane transport). The electrical conductivity $\sigma_{e,xx}$ is expected to be about three times lower (see Fig. 5c) than in the other directions.

Figs. 6 (left column) show *p*-type DOS effective mass in function of the carrier concentration and temperature. The LT structure, already at $n = 10^{18} \text{ cm}^{-3}$, has considerably large value of the 'bare' mass (i.e. not affected by temperature blurring, $T = 15 \text{ K}$ curve), $m^* \simeq 1.0$, which is raising significantly above $n = 2 \times 10^{19} \text{ cm}^{-3}$. At $T = 300 \text{ K}$, similarly to the *n*-type doping, critical concentration, where additional bands start to have influence on m^* , is blurred, and m^* is almost constant ($m^* \simeq 1.5$) up to 10^{20} cm^{-3} , then rising to $3 m_e$ at $n = 10^{21} \text{ cm}^{-3}$. At higher temperatures, the deep and heavy valence bands contribute to the effective mass even at the lowest concentrations, however, we have to keep in mind, that integral in Eq.12 covers carriers being far from the gap, where bands are generally not parabolic, thus the characterization of bands in terms of the effective mass may become inaccurate.

Closing the effective mass discussion, for all the LT, MT and HT cases, *n*-type effective masses are smaller than *p*-type.

B. Transport properties

1. Thermopower

Thermopower as a function of electrons/holes concentration for the three different temperatures are presented in Fig. 7 where data for the different temperatures were

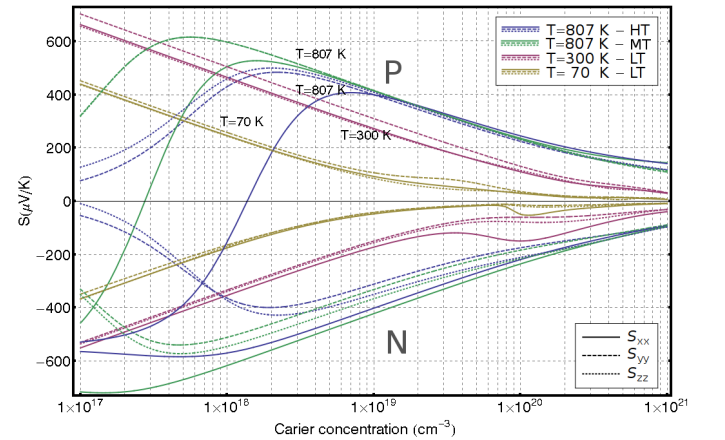


FIG. 7: (Color online) Thermopower, in function of the carrier concentration, for the *p*- (top panel) and *n*-type (bottom panel) SnSe, for $T = 70 \text{ K}$, 300 K and 807 K . The electronic band structures of different phases were used to calculate thermopower: LT at 70 K and 300 K , MT and HT at 807 K .

obtained for the corresponding crystal structures. The complete results for all the phases at all the temperatures are shown in the Appendix B. The most interesting features are seen for the n -type LT case, that exhibits strong anisotropy of the Seebeck coefficient, visible at $T = 70$ and 300 K around $n \sim 10^{20} \text{ cm}^{-3}$. The n -type S_{xx} tensor element has the largest absolute value; at low temperatures S_{xx} starts to dominate at $1 \times 10^{20} \text{ cm}^{-3}$, where the Fermi energy reaches 5 electron pockets with high v_x (see, red line in Fig.5b). At higher temperatures (i.e. for MT and HT), around $n \sim 2 \times 10^{19} \text{ cm}^{-3}$, E_F reaches only one additional electron pocket (see, Fig. 5d,f, red line), and the advantage of reaching this pocket spreads over wider concentrations range (see, n -type S_{xx} at 807 K in Fig. 7). This is reflected as $\sim 20\%$ rise of S_{xx} thermopower in the whole concentrations range.

The anisotropy of p -type thermopower is less significant. Similar enhancement of the thermopower, as observed for the n -type, caused by the appearance of additional bands near the Fermi level, is seen in p -type S_{yy} component at $p \approx 3 \times 10^{19} \text{ cm}^{-3}$. Two, non-parabolic pockets, have a high velocity of electrons in y -direction, increasing rapidly at $p \approx 3 \times 10^{19} \text{ cm}^{-3}$, which provides the increase of σ_{yy} derivative (see, green line in Fig. 5a). Significance of this effect is smaller, than in the n -type doping, and seen only in the LT phase, but it is sufficient to provide an increase of S_{yy} over S_{xx} and S_{zz} (best seen at 300 K).

As far as the bipolar effects are concerned, we can observe, that p -type S_{xx} element shows the strongest reduction at the high temperature, which is caused by the large n -type S_{xx} and σ_{xx} . The major detrimental effect at high temperatures is related to the reduction of the band gap during the phase transition (LT and MT vs HT, see Table II). To visualize this influence of the gap reduction on the bipolar effect, we have plotted S at the same temperature of 807 K (phase transition temperature) computed for the MT and HT cases. Much smaller band gap in the HT phase leads to the much stronger bipolar effect, and the thermopower starts to decrease already for $p < 10^{19} \text{ cm}^{-3}$ and $n < 2 \times 10^{18} \text{ cm}^{-3}$. Note also, that the bipolar effect critically depends on the value of the band gap, which here for the HT phase was adjusted in an approximate way, since we are not aware of the experimental value.

Isotropic thermopower, calculated using Eq. 5, is shown as a color map in Fig. 8, and $S(T)$ curves for selected carrier concentrations are collected in Appendix B, Fig. 16. To allow for a comparison between the different phases, all three cases for complete temperature ranges are displayed. After averaging over three directions, in all the three phases, p -type thermopower is generally larger than n -type one. For n -type LT map, around $n \sim 10^{20} \text{ cm}^{-3}$, and below 400 K, we observe the abnormal bending of S , which increases with the carrier concentration. This is due to the rise in S_{xx} element, discussed before. For the MT and HT phases, such effect is not observed, and the variation of S with the carrier

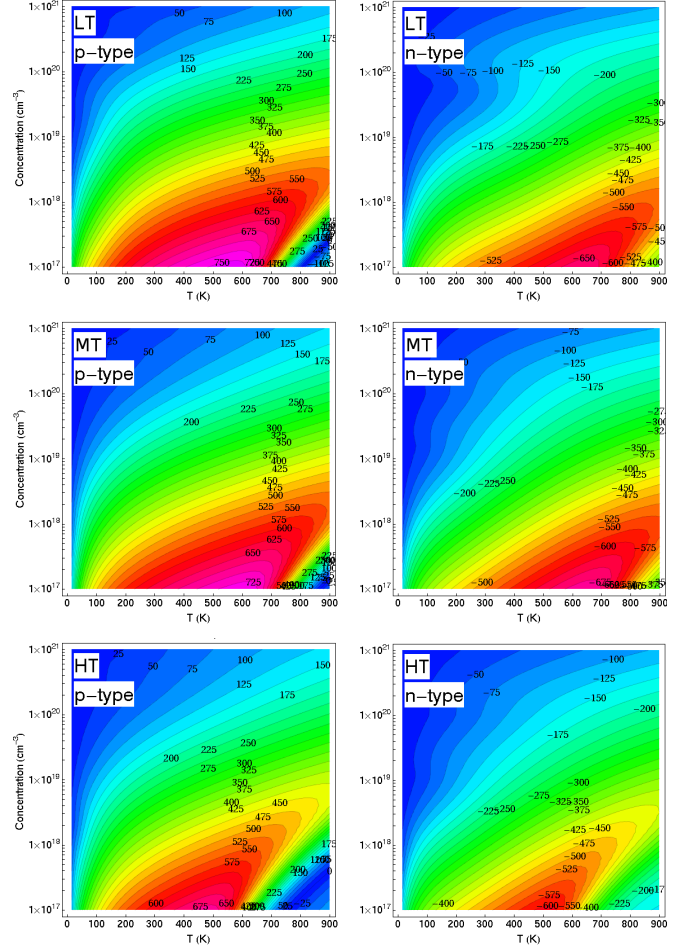


FIG. 8: (Color online) Isotropic thermopower for LT, MT, and HT phases of SnSe (see Tab. I) for n - and p -type doping.

concentration is monotonic (S decreases with n or p). At the highest temperatures and the lowest carrier concentrations, we again observe a drop of S due to the bipolar effects, the strongest for the p -type HT phase.

2. Power factor

The power factor ($\text{PF} = S^2/\sigma$), similarly to the electrical conductivity, cannot be directly calculated if the electronic relaxation time τ is not known, however the discussion of PF/τ can be still very useful in optimizing the carrier concentration in the SnSe system. For completeness of the analysis, we show results for all the phases (LT, MT and HT) at $T = 450$ and 807 K, although one has to bear in mind that these phases describe SnSe in limited temperature ranges.

Results of the calculations are shown in Fig. 9. The most striking observation is, that for the p -type SnSe, xx tensor element of the power factor (PF_{xx}) is the smallest one, in contrast to the n -type, where PF_{xx} is the largest.

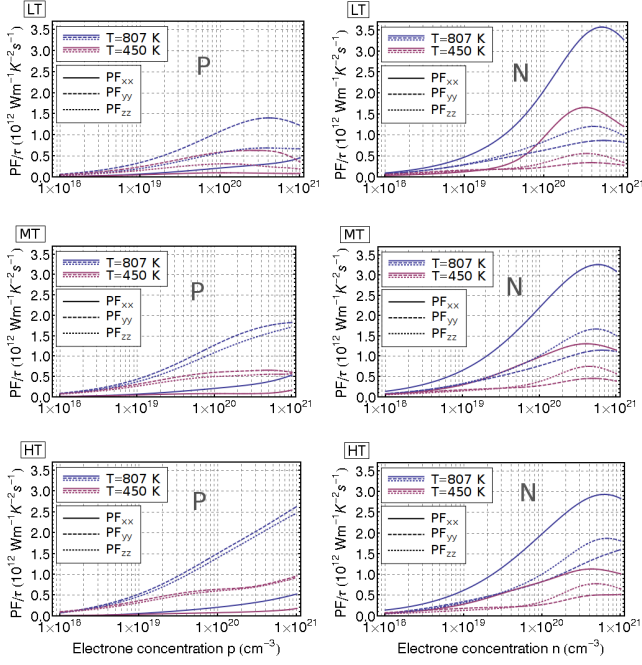


FIG. 9: (Color online) Power factor of the LT, MT and HT phases for *p*- (left column) and *n*-type (right column) SnSe in function of concentration for two temperatures (450 K and 807 K), calculated along three directions.

The reason is that in the *p*-type, *x*-direction inter-layer conducting channel is blocked due to the smallest TF (see, Fig. 5, red line), whereas in the *n*-type, it is activated by the electron pockets with high v_x . The smallest *p*-type PF_{xx} , comparing to *y*- and *z*-directions, remains in agreement with the experimental findings¹.

In the *p*-type LT phase, value of the thermopower is approximately isotropic (except for S_{xx} at low concentrations), thus overall anisotropy in the PF is due to the electrical conductivity: transport function element σ_{yy}/τ has the biggest value (in $p > 5 \times 10^{19} \text{ cm}^{-3}$) which makes PF the largest in the *y*-direction. For the high temperature structures, namely MT and HT, the power factor for *y*- and *z*-directions becomes similar, and is the largest for the HT phase. In the *n*-type SnSe, PF/τ curves look quite similar, while comparing the LT, MT and HT cases, with decreasing anisotropy (measured as PF_{xx}/PF_{yy} and PF_{xx}/PF_{zz}) upon going from LT to HT.

For isotropic (polycrystalline) material, the power factor, calculated using Eq. 6, is mapped in Fig. 10. The first observation is, that generally the *n*-type SnSe has larger values of PFs, than the *p*-type one, thus the heavily doped *n*-type SnSe can exhibit even better thermoelectric performance, and better polycrystalline zT over the broad temperature range. It seems that the existence of the structural phase transition is beneficial for the power factor value only for *p*-type SnSe, where HT phase exhibits the largest values, but only for large carrier concentrations, where the bipolar effects are not so

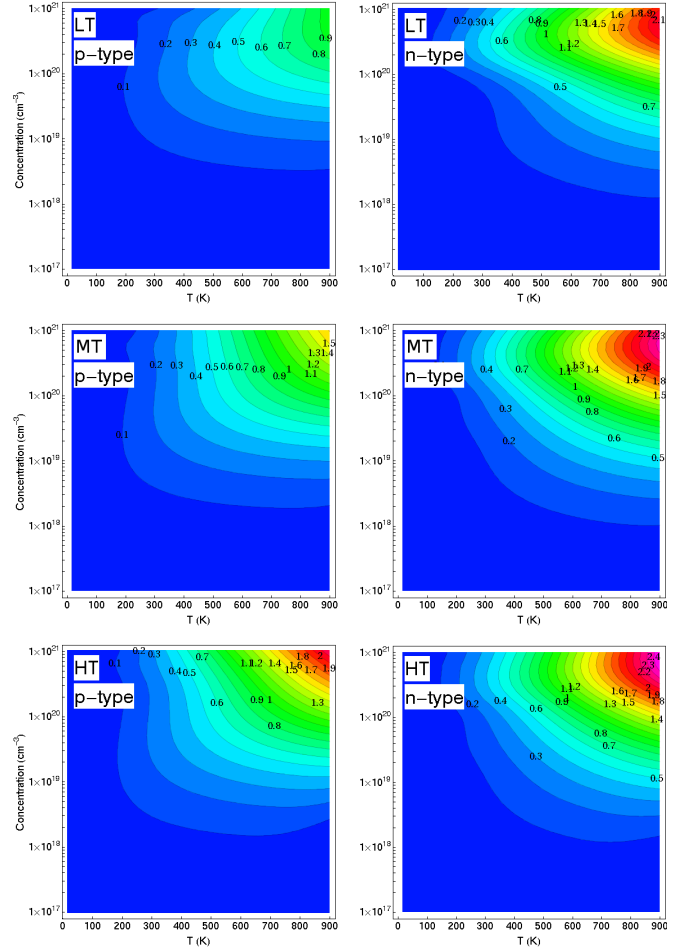


FIG. 10: (Color online) Isotropic power factor for *n*- and *p*-type SnSe (LT, MT and HT phases) in function of the carrier concentration and temperature. All values in $10^{12} \text{ W K}^{-2} \text{ m}^{-1} \text{ s}^{-1}$.

important. However, at higher concentrations, the zT value may not benefit from the phase transition, because of the increasing contribution of the electronic part of the thermal conductivity.

The maps of PF also reveal that SnSe is best suited for TE application at temperatures $T > 600 \text{ K}$ and should be rather heavily doped, for both *n*- and *p*-type above 10^{20} cm^{-3} .

Note, that all the presented transport calculations results and predictions are based on the constant relaxation time approximation, and, in principle, electron-phonon or electron-impurity scattering may markedly affect them. Especially for the case, where both heavy, and light electrons are involved in electrical transport, scattering effects may be of increased importance, due to the different scattering rates for these two electronic bands.

C. Comparison with experiment

Experimental data were taken from Ref. 1, where the transport properties of the single crystal *p*-type SnSe were reported. Since our calculations were performed within the constant relaxation time approximation, only thermopower can be directly compared. Fig. 11 shows the measured Seebeck coefficient along *a*, *b*, and *c* crystallographic directions³⁰ compared with two sets of corresponding theoretical values, for hole concentrations $p = 3 \times 10^{17}$ and $7 \times 10^{17} \text{ cm}^{-3}$. These carrier concentrations were selected for comparison basing on the measured Hall coefficient of SnSe at $T = 300 \text{ K}$, depicted also in Fig. 12a. Nevertheless, one has to bear in mind that due to the anisotropic crystal structure and Fermi surface, as well as the strongly non-parabolic band structure, Hall coefficient data do not reflect directly the carrier concentration. In Fig. 11 we see, that the experimental Seebeck coefficient well matches the theoretical values below 600 K, for $p = 7 \times 10^{17} \text{ cm}^{-3}$, and then is underestimated in the mid-temperature range ($\sim 700 \text{ K}$). The most intriguing experimental behavior is noticed for the thermopower, which remains constant with temperature above T_c . For such high temperatures, and carrier concentration around $p \sim 10^{17} \text{ cm}^{-3}$, bipolar effect should strongly decrease S , even making S negative, as seen from our computations, shown in Fig. 7 and Fig. 16. Similar observations, with even faster decreasing S due to the smaller band gap, were reported from calculations in Ref. 9.

One can attempt to explain such an uncommon situation assuming the gradual increase of the carrier concentration with temperature, since it could explain both, the decrease in S above 600 K, and saturation of S above 800 K, with almost invisible bipolar effect. Experimental Hall measurements also show, that $1/R_H$ rises almost two order of magnitudes (see, Fig. 12a), between 600 and 800 K, which supports the above-mentioned hypothesis. Moreover, for the high carrier concentration, the thermopower changes smoothly while crossing the phase transition temperature. Fig. 7 shows that only concentrations larger than $1 \times 10^{19} \text{ cm}^{-3}$ provide similar Seebeck coefficient at $T = 807 \text{ K}$ for MT and HT phases. Finally, measured electrical conductivity (see, Ref. 1) shows non-monotonic behavior with increasing temperature, i.e. it decreases from 300 K to 550 K, increases above 550 K and becomes constant above T_c . Such a trend remains in line with the expectation of increasing carrier concentration above 550 K, where the experimental and theoretical thermopower starts to deviate.

To partly verify this hypothesis, we have plotted how carrier concentration should change with temperature, to reach the agreement between the experimental and calculated thermopowers.³¹ As we can see in Fig. 12b, the unusual, experimental behavior of thermopower, directly results in the rising carrier concentration in SnSe, to more than $1 \times 10^{19} \text{ cm}^{-3}$ around 800 K, and the measured inverse Hall resistivity (Fig. 12a), exhibits similar

temperature dependence to our extracted $p(T)$ function.

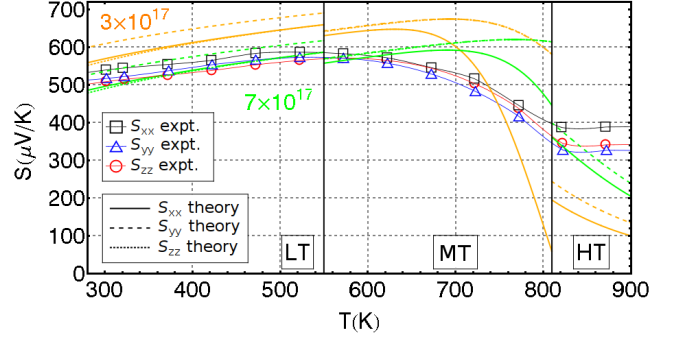


FIG. 11: (Color online) Comparison of the calculated and experimental values¹ of the thermopower vs. temperature. Nominal hole concentrations for the theoretical curves are 3×10^{17} (orange) and $7 \times 10^{17} \text{ cm}^{-3}$ (green).

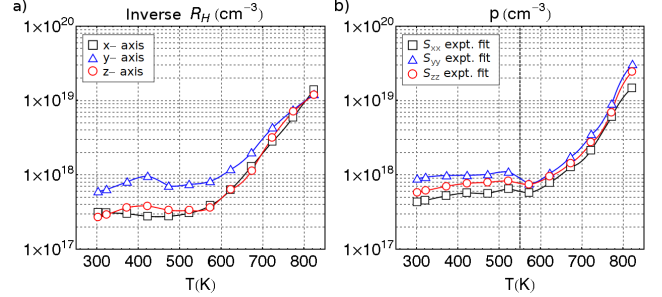


FIG. 12: (Color online) (a) Concentration derived from the measured Hall coefficient, according to $n_H = 1/eR_H$; (b) nominal carrier concentration at which the calculated thermopower equals to the experimental value. All concentrations are given in cm^{-3} , experimental data are taken from Ref. 1. Vertical line separates the temperature ranges, where theoretical thermopower of LT (below 550 K) and MT (above 550 K) phases was used.

IV. SUMMARY

Electronic structure and thermoelectric properties of *n* and *p*-type SnSe were studied, using the KKR method and the Boltzmann transport approach, within the constant relaxation time approximation. We have shown, that the temperature evolution of the crystal structure within the *Pnma* phase (i.e. before reaching the structural phase transition at 807 K), leads to the significant changes in the electronic band structure. On the other hand, the phase transition, occurring at 807 K, leads mainly to the abrupt change of the energy band gap value, whereas modifications of $\mathcal{E}(\mathbf{k})$ curves are minor.

The effective masses, analyzed in function of the carrier concentration and temperature, indicate, that overall p -type masses are larger than n -type ones, and SnSe exhibits strong anisotropy of the electron transport properties for both types of charge conductivity.

P -type SnSe, computed for the room temperature crystal structure parameters, has strongly non-parabolic dispersion relations, with the 'pudding-mold'-like shape of the highest valence band. Due to the flat bands, yielding large effective masses, the inter-layer electron transport seems to be blocked, resulting in small power factor and Seebeck coefficients, when comparing with the corresponding values computed for the other directions (i.e. in-plane electron transport).

The opposite situation was found in the n -type SnSe, where the inter-layer direction exhibits band structure features, highly beneficial for thermoelectric performance. In this case, when critical concentration between 10^{19} cm^{-3} (HT) - 10^{20} cm^{-3} (LT, see, Fig. 5) is reached, or when high velocity electron band is thermally activated at high temperatures, two types of carriers are present simultaneously in the system, i.e. more localized electrons, having large effective masses, and highly mobile electrons, possessing low effective masses and high velocity. This particular combination results in high thermopower and power factor in the inter-layer direction. In view of our results, the n -type SnSe may be even better thermoelectric material, than the p -type one.

Our theoretical study confirmed the strong anisotropy of the electron transport in SnSe. This results in the much worse thermoelectric performance in the polycrystalline material, in agreement with the experimental reports^{7,8}.

On the whole, the computational results, derived from the KKR method and Boltzmann equations, show quite good agreement with the measured data¹ below $T \sim 600 \text{ K}$. The experimentally observed changes in S , σ and R_H for $T > 600 \text{ K}$ suggest, that in the measured SnSe samples, the carrier concentration was gradually increasing, and the discrepancy between the theoretical and measured Seebeck coefficient, appearing at high temperatures ($T > 600 \text{ K}$) can be corrected when the actual Hall concentration is taken into account in calculations. Nevertheless, the mechanism responsible for such a generation of additional carriers, suggested in our discussion, remains unknown.

Appendix A: Polycrystalline random grain model

In a polycrystalline material, where grains have different crystalline orientation and are randomly distributed, the effective Seebeck coefficient, as well as the power factor, are not simple averages of the single grain properties. To obtain the correct isotropic values, appropriate circuit model for thermoelectric generator is build (see Fig. 13).

In the polycrystalline sample it is assumed, that the material consists of three types of small grains, with

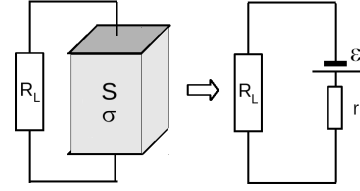


FIG. 13: Circuit model of lumped (with R_L) thermoelectric material.

thermopower S_k ($k = 1, 2, 3$) each, and electrical conductivities σ_k (see Fig. 14), distributed on a regular grid. This model can be simplified to the thermoelectric module made from three solid materials connected in parallel. On this basis, equivalent circuit model was made.

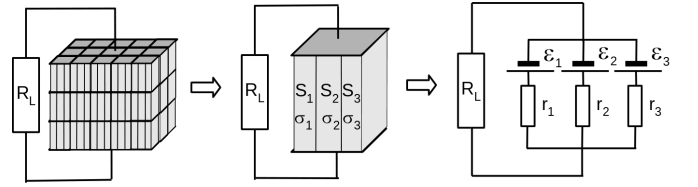


FIG. 14: Model of the thermoelectric material, which is build up from three types of small, randomly distributed grains, with different transport properties.

The thermoelectric module with one the type of material, having the thermopower S and electrical conductivity σ , can be replaced with the electromotive force (emf) $\mathcal{E} = S\Delta T$ and $r = \sigma l/A$, where l and A are length, and cross section of the module, respectively (see Fig. 13). Effective thermopower can be defined as voltage on the module, divided by the temperature difference ΔT , when R_L goes to infinity.

$$S_{eff} = \frac{U}{\Delta T} = \frac{iR_L}{\Delta T} = \frac{\mathcal{E}}{r + R_L} \frac{R_L}{\Delta T} \xrightarrow{R_L \rightarrow \infty} \frac{\mathcal{E}}{\Delta T} = S \quad (\text{A1})$$

where i is the current in circuit.

The power factor can be defined as a capability of energy production of material with the cross section A , and length l , at the given temperature difference ΔT

$$PF_{eff} = \frac{Pl}{A\Delta T^2}, \quad (\text{A2})$$

where P is the power output of the source, when R_L goes to zero (short circuit power).

$$P = \mathcal{E}i = \frac{\mathcal{E}^2}{r + R_L} \xrightarrow{R_L \rightarrow 0} \frac{\mathcal{E}^2}{r} \quad (\text{A3})$$

and therefore

$$PF_{eff} = \frac{Pl}{A\Delta T^2} = \left(\frac{\mathcal{E}}{\Delta T} \right)^2 \frac{l}{Ar} = S^2 \sigma, \quad (\text{A4})$$

In case of the equivalent polycrystalline circuit model, the effective thermopower is:

$$S_{eff} = \frac{U}{\Delta T} = \frac{iR_L}{\Delta T}. \quad (A5)$$

From circuit theory

$$i_k = \frac{\mathcal{E}_k - iR_L}{r_k} \quad \text{and} \quad i = \sum_k i_k \quad (A6)$$

where k is 1, 2, 3. Now i can be found

$$i = \frac{\sum_k \mathcal{E}_k / r_k}{R_L \sum_k 1/r_k + 1}. \quad (A7)$$

$$\begin{aligned} S_{eff} &= \frac{iR_L}{\Delta T} = \frac{\sum_k \mathcal{E}_k / r_k}{R_L \sum_k 1/r_k + 1/R_L} \frac{1}{\Delta T} \xrightarrow{R_L \rightarrow \infty} \\ &= \frac{\sum_k \mathcal{E}_k / r_k}{\sum_k 1/r_k} \frac{1}{\Delta T} = \frac{\sum_k S_k \sigma_k}{\sum_k \sigma_k}. \end{aligned} \quad (A8)$$

Power of the source is now a sum of powers of all the sources

$$P = \sum_k \mathcal{E}_k i = \frac{\mathcal{E}_k^2 - i\mathcal{E}_k R_L}{r_k} \xrightarrow{R_L \rightarrow 0} = \sum_k \frac{\mathcal{E}_k^2}{r_k} \quad (A9)$$

and therefore

$$PF_{eff} = \frac{Pl}{A\Delta T^2} = \sum_k \left(\frac{\mathcal{E}_k}{\Delta T} \right)^2 \frac{l}{A_k r_k} = \frac{1}{3} \sum_k S_k^2 \sigma_k, \quad (A10)$$

where $A_k = 1/3A$ (grains are randomly distributed).

Appendix B: Extended data

In this Appendix, additional figures are included, showing the complete data for the anisotropic (Fig. 15) and isotropic (Fig. 16) thermopowers of the three considered SnSe structures.

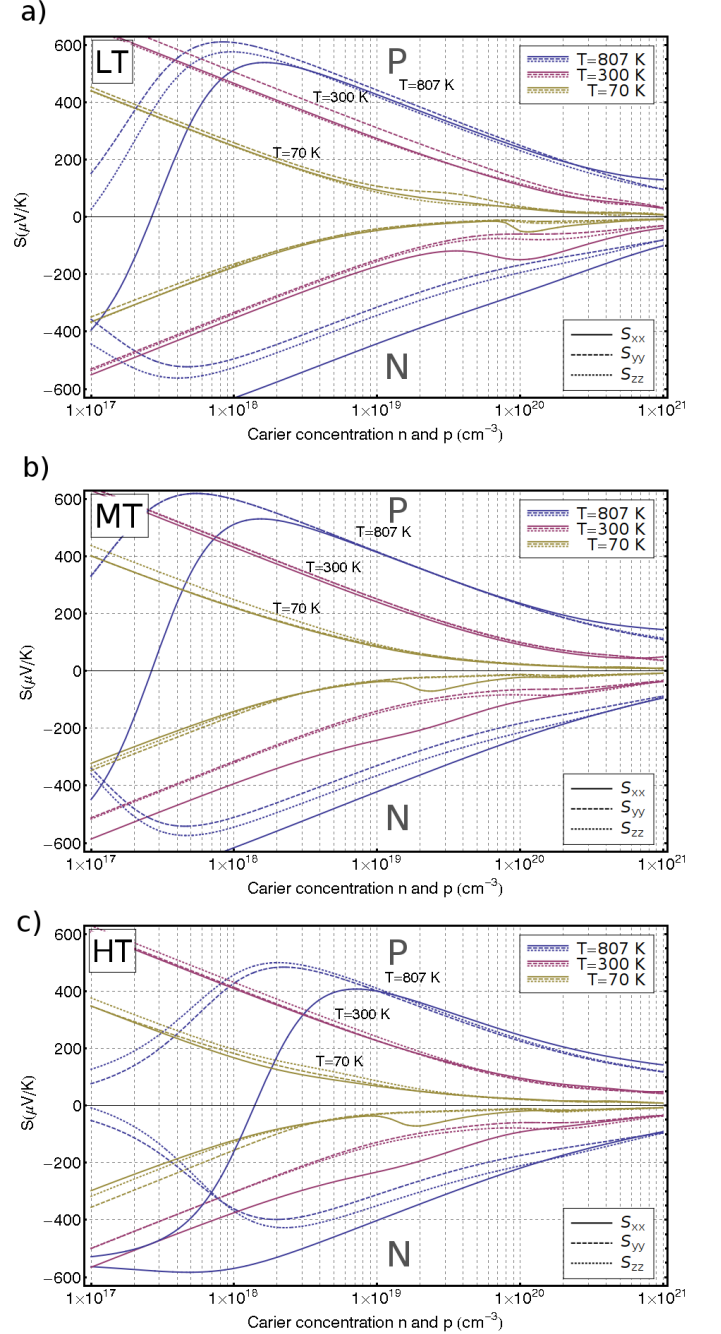


FIG. 15: (Color online) Thermopower LT (a), MT (b) and HT (c) phases at three different temperature and crystallographic direction.

Acknowledgments

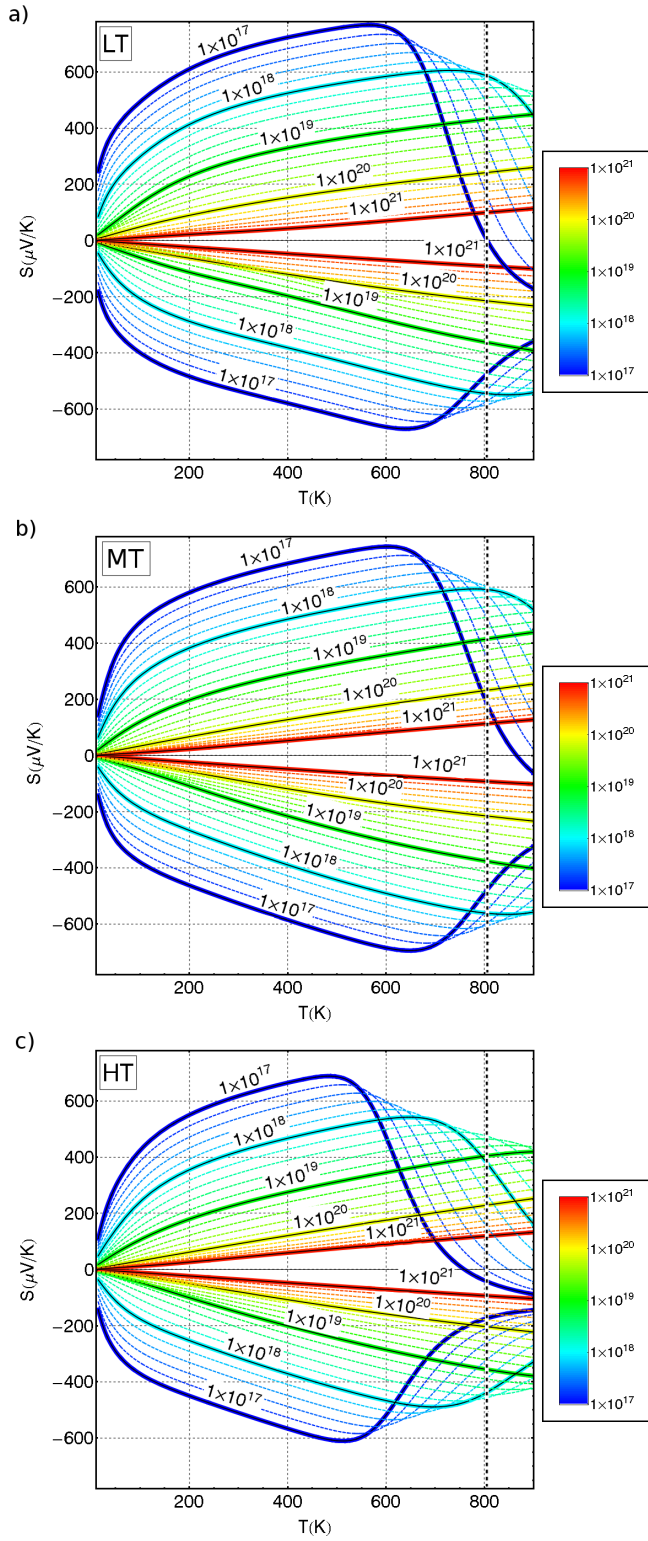


FIG. 16: (Color online) Isotropic thermopower in function of temperature for LT (a), MT (b) and HT (c) for the n and p -type doping. Different color lines correspond to the different carrier concentrations. Thick line marks concentrations in cm^{-3} .

This work was supported by the Polish National Science Center (NCN) under the grants DEC-2011/02/A/ST3/00124 and partially by the Polish Ministry of Science and Higher Education.

-
- * kamil.kutorasinski@fis.agh.edu.pl
- ¹ Li-Dong Zhao, Shih-Han Lo, Yongsheng Zhang, Hui Sun, Gangjian Tan, Ctirad Uher, C. Wolverton, Vinayak P. Dravid, and Mercouri G. Kanatzidis, *Nature*, **508**, 373 (2014)
 - ² P. P. Heremans, V. Jovovic, E. S. Toberer, A. Saramat, k. Kurosaki, A. Charoenphakdee, S. Yamanaka and G. J. Snyder, *Science* **321**, 554 (2008).
 - ³ Y. Pei, X. Shi, A. LaLonde, H. Wang, L. Chen and G. J. Snyder, *Nature* **473**, 66 (2011).
 - ⁴ P. Dziawa, B. J. Kowalski, K. Dybko, R. Buczko, A. Szczerbakow, M. Szot, E. Lusakowska, T. Balasubramanian, B. M. Wojek, M. H. Berntsen, O. Tjernberg and T. Story, *Nature Mat.* **11**, 1023 (2012).
 - ⁵ Dong-Xia Qu, Y. S. Hor, Jun Xiong, R. J. Cava, and N. P. Ong, *Science* **329**, 821 (2010).
 - ⁶ T. Chattopadhyay, J. Pannetier and H. G. Von Schnering, *J. Phys. Chem. Solids* **47**, 879 (1986).
 - ⁷ S. Sassi, C. Candolfi, J.-B. Vaney, V. Ohorodniichuk, P. Masschelein, A. Dauscher and B. Lenoir, *Appl. Phys. Lett.* **104**, 212105 (2014).
 - ⁸ Cheng-Lung Chen, Heng Wang, Yang-Yuan Chen, Tristan Daya and G. Jeffrey Snyder, *J. Mater. Chem. A* **2**, 11171 (2014).
 - ⁹ G. Shi, E. Kioupakis, *J. Appl. Phys.* **117**, 065103 (2015)
 - ¹⁰ N.W. Ashcroft N.D. Mermin *Solid State Physics*, 1976
 - ¹¹ T. Thonhauser, T. J. Scheidemantel, J. O. Sofo, J. V. Badding, and G. D. Mahan, *Phys. Rev. B* **68**, 085201 (2003).
 - ¹² G. K. H. Madsen, K. Schwarz, P. Blaha, and D. J. Singh, *Phys. Rev. B* **68**, 125212 (2003)
 - ¹³ K. Kutorasinski, J. Tobola, and S. Kaprzyk, *Phys. Rev. B* **87**, 195205 (2013)
 - ¹⁴ L. Chaput, P. Pecheur, J. Tobola, and H. Scherrer, *Phys. Rev. B* **72**, 085126 (2005)
 - ¹⁵ K. Kutorasinski, B. Wiendlocha, J. Tobola, and S. Kaprzyk, *Phys. Rev. B* **89**, 115205 (2014)
 - ¹⁶ H. Kohn and N. Rostoker *Phys. Rev.* **94** 1111 (1954)
 - ¹⁷ W. H. Butler *Phys. Rev. B* **14** 468 (1976)
 - ¹⁸ S. Kaprzyk and A. Bansil *Phys. Rev. B* **26**, 367 (1982)
 - ¹⁹ S. Kaprzyk and A. Bansil *Phys. Rev. B* **42**, 7358 (1990)
 - ²⁰ A. Bansil, S. Kaprzyk, P. E. Mijnders and J. Tobola, *Phys. Rev. B* **60**, 13396 (1999).
 - ²¹ T. Stopa, S. Kaprzyk, J. Tobola *J. Phys.: Condens. Matter* **16**, 4921 (2004)
 - ²² D.D. Koelling and B.N. Harmon *J. Phys.C: Solid State Phys* **10** 3107 (1977)
 - ²³ H. Ebert, H. Freyer and M. Deng, *Phys. Rev. B* **56**, 9454 (1997)
 - ²⁴ W. E. Lorensen, *Computer Graphics*, Vol. **21**, Nr. 4, July 1987
 - ²⁵ H. Gouraud, *IEEE Transactions on Computers* **100**, 623-629 (1971)
 - ²⁶ E. A. Stern *Phys. Rev.* **157** 544 (1967)
 - ²⁷ J. P. Perdew and Y. Wang *Phys. Rev. B* **45**, 13244 (1992)
 - ²⁸ K. Kuroki, and R. Arita, *J. Phys. Soc. Jpn.* **76**, 083707 (2007)
 - ²⁹ We use the term *phase* to name the three different crystal unit cells of SnSe, even if, in fact, LT and MT have the same space group, so are not exactly different crystalline phases.
 - ³⁰ The original data from Ref. 1 were transformed to our convention of the unit cell axes. In Ref.1 axes *c* is the shortest one, thus *b* and *c* are exchanged, comparing to our convention of Pnma.
 - ³¹ Carrier concentration *p* is extracted, applying the condition, that $S_{\text{expt.}}(T) = S_{\text{theor.}}(p, T)$ at every *T*.